Aalborg Universitet

AALBORG UNIVERSITY

DENMARK

Water- and air-filled pore networks and transport parameters under drying and wetting processes

Hamamoto, Shoichiro; Ohko, Yushi; Ohtake, Yutaka; Moldrup, Per; Nishimura, Taku

ORIGINAL RESEARCH ARTICLE

Water- and air-filled pore networks and transport parameters under drying and wetting processes

Shoichiro Hamamoto[1] | **Yushi Ohko**[1] | **Yutaka Ohtake**[2] | **Per Moldrup**[3] |
Taku Nishimura[1]

[1]Graduate School of Agricultural and Life
Sciences, The Univ. of Tokyo, 1-1-1, Yayoi,
Bunkyoku, Tokyo 113-8657, Japan

[2]Graduate School of Engineering, The Univ.
of Tokyo, 7-3-1, Hongo, Bunkyoku, Tokyo
113-8657, Japan

[3]Dep. of the Built Environment, Aalborg
Univ., Thomas Manns Vej 23, Aalborg East
9220, Denmark

Correspondence
Shoichiro Hamamoto, Graduate School of
Agricultural and Life Sciences, The Univ. of
Tokyo, 1-1-1, Yayoi, Bunkyoku, Tokyo,
113-8657, Japan.
Email: shoichi@soil.en.a.u-tokyo.ac.jp

Assigned to Associate Editor Muhammad
Naveed.

Abstract

The connectivity and tortuosity of fluid-filled pore networks in the water and air phases strongly influence the mass transport in porous media. Moisture conditions (water content and distribution) alter water- or air-filled pore networks. In this study, using a sand column with variable saturated conditions, water- and air-filled pore networks were analyzed using X-ray computed tomography (CT). Water and air transport parameters, including hydraulic conductivity, gas diffusion coefficient, and air permeability, were measured. The objectives were (a) to identify the effects of entrapped air on the water-filled pore network and hydraulic conductivity and (b) to understand the water- and air-filled pore networks and relevant transport parameters in the sand column during the drying and wetting processes. Measurements of hydraulic conductivity using quasisaturated samples showed that hydraulic conductivity was drastically reduced when smaller in situ air bubbles were present inside the sand column. At the same air-filled porosity, higher gas diffusivity and air permeability were obtained under wetting than those during drying. X-ray CT image analysis revealed that the air-filled pore network connectivity during wetting was higher than that during drying, resulting in enhanced gas transport parameters during the wetting process. The observed differences in water- and air-filled pore networks during drying and wetting processes are highly promising for future multiphase mass transport models in soils.

1 | INTRODUCTION

Many agricultural and engineering applications require knowledge of mass and energy transport in soils, which occurs through pore networks with complex geometries and connectivities. Moisture conditions (water content and distribution) are expected to significantly influence the fluid-filled pore network, such as the pore size distribution, pore network tortuosity, and pore network coordination number of air- or water-filled pores. Soil moisture levels are classified as fol-

lows: (a) fully saturated conditions without any air phase, (b) quasisaturated conditions with isolated air bubbles trapped inside the pore bodies, and (c) unsaturated conditions with a continuous air phase connected to the atmosphere. The entrapped air, which is attributed to biogenic gas production, groundwater table fluctuations, and temperature disturbance in groundwater (Ryan et al., 2000), reduces hydraulic conductivity without substantially reducing volumetric water content (Faybishenko, 1995; Fry et al., 1997; Marinas et al., 2013; Ronen et al., 1989; Sakaguchi et al., 2005). Fry et al. (1997) investigated the effects of entrapped air on the hydraulic

Abbreviations: CT, computed tomography.

conductivity of repacked sand. Entrapped air was produced using three emplacement methods: direct gas injection, injection of water supersaturated with gas, and injection of an H_2O_2 solution. They revealed that hydraulic conductivity is proportional to the volume of the gas phase and is unaffected by the emplacement method. Thus, the reduction in hydraulic conductivity by entrapped air has been extensively studied in numerous studies. However, most studies have not characterized the entrapped air (i.e., bubble size and its distribution) or the changes in the water-filled pore network induced by the entrapped air. Further studies are required to understand the effects of entrapped air on hydraulic properties, which are important for managing groundwater systems, including irrigation and drainage systems, injection of water in the vadose zone, remediation of polluted sites using air barriers, and artificial groundwater recharge (Faybishenko, 1995).

Water retention hysteresis is a well-known phenomenon in the relationship between volumetric water content and suction. Hydraulic conductivity is generally greater during the drying process (where the volumetric water content is greater) than during the wetting process for the same magnitude of suction, with only minor hysteresis observed in the relationship between hydraulic conductivity and volumetric water content (Gallage et al., 2013; Mualem, 1986; Topp, 1971). Gas transport parameters, particularly air permeability, also exhibit hysteresis in suction (Dury et al., 1998; Stonestrom & Rubin, 1989). In contrast with unsaturated hydraulic conductivity, these studies also showed a difference in air permeability at a similar water saturation (i.e., air-filled porosity) during the drying and wetting processes. Thus, the pore networks in the water and air phases during drying and wetting processes differ significantly.

X-ray computed tomography (CT) is well known for its effectiveness in characterizing three-dimensional soil pore geometry. X-ray CT analysis enables quantification of the pore network. For example, X-ray CT analysis can provide pore network information such as porosity (Anderson et al., 1990; Rachman et al., 2005), pore size distribution (Lindquist et al., 2000), pore network tortuosity and connectivity (Lindquist et al., 1996; Müller et al., 2018; Naveed et al., 2013), and pore network coordination number (Hamamoto et al., 2016). Several studies have linked pore networks and mass-transport parameters (Baniya et al., 2019; Hamamoto et al., 2016; Müller et al., 2018; Naveed et al., 2013). Müller et al. (2018) used X-ray CT to characterize the macropore network in Andosol and Gleysol and investigated the relationship between the obtained pore network parameters, such as microporosity, macropore size, or macropore network connectivity, and unsaturated hydraulic conductivity at different suctions. Unsaturated hydraulic conductivity and total microporosity were found to have a positive relationship in both soils. Additionally, predictive models for mass transport parameters based on pore network parameters derived

Core Ideas

- Hydraulic conductivity was drastically reduced when smaller in situ air bubbles were present inside sand column.
- Higher gas transport parameters were obtained for unsaturated sand under wetting than under drying process.
- Higher pore network connectivity in the air phase was created under wetting than under drying process.

from X-ray CT images have been proposed (Baniya et al., 2019; Hamamoto et al., 2016). These studies clearly suggest that pore structure analysis based on X-ray CT analysis is important for understanding mass transport processes in soils. However, only a few studies have separately characterized pore networks in the water and air phases of the same material at different moisture levels, and we still lack a fundamental understanding of pore network characteristics in each phase and their relationship to mass (water and gas) transport parameters. These are useful for the further development of improved and more realistic predictive models for mass transport parameters considering the pore network structure.

In this study, sand was used as a porous medium with varying saturated conditions, including quasisaturated and unsaturated conditions during drying and wetting processes. The pore network characteristics in the water and air phases were analyzed using X-ray CT, and mass transport parameters, including hydraulic conductivity, gas diffusion coefficient, and air permeability, were measured. The objectives were (a) to identify the effects of entrapped air on the water-phase pore network and hydraulic conductivity and (b) to understand the water- and air-filled pore networks and relevant transport parameters in the sand column during the drying and wetting processes.

2 | MATERIALS AND METHODS

2.1 | Materials and sample columns

Toyoura sand was used as a porous medium. The particle sizes ranged from 0.02 to 0.42 mm. Sand with a bulk density of 1.52 g cm^{-3} (a total porosity of approximately 0.42 cm^3 cm^{-3}) was repacked into a stainless or acrylic column for the measurements of mass transport parameters and X-ray CT images. An acrylic column was used for the X-ray CT measurements by considering the X-ray transmission. A stainless steel column with a height of 5.1 cm and diameter of 5.0 cm

was used for the measurements of saturated and quasisaturated hydraulic conductivities, gas diffusion coefficient, and air permeability. Acrylic columns, one of 6.5-cm height and 4.6-cm diameter and one of 5.2-cm height and 1.0-cm diameter, were used for the measurements of unsaturated hydraulic conductivity and X-ray CT images, respectively.

2.2 | Preparations for sands with fully saturated and quasisaturated conditions

Fully saturated samples were prepared by repacking dry sand into a column under degassed water. Quasisaturated samples were prepared in two ways: (a) H_2O_2 samples, where dry sand was repacked into the column under different concentrations of H_2O_2 solution (0.1, 0.03, and 0.05%) and kept for 1 d in a climate-controlled room at 20 °C, creating spontaneous bubbles inside the media, and resulting in a variable volume fraction of entrapped air (ω, $cm^3\ cm^{-3}$) ranging from 0.05 to 0.11; and (b) resaturated samples, where fully saturated samples were drained from the bottom of the column by applying suction of 70 cmH_2O and resaturated again by immersing the whole column into the water. The variable time for drainage before resaturation was applied to the resaturated samples to obtain variable ω ranging from 0.06 to 0.11. For the H_2O_2 samples used for X-ray CT images, a 0.05% H_2O_2 solution was used to obtain $\omega = 0.06$, which was comparable to that of the resaturated samples.

2.3 | Preparations for sand during drying and wetting processes

Unsaturated sand columns for mass transport parameters were prepared by applying different suctions to the fully saturated samples. Suction was applied to the bottom of the column using a water drainage tube and was increased at intervals of 5 cmH_2O up to 70 cmH_2O (drying process) by controlling the height between the sand column and drainage point. After 70 cmH_2O, the samples were rewetted by decreasing the suction at the same interval (wetting process) by adjusting the drainage point. The following suction was applied to the column in each drying and wetting process for the unsaturated samples in the X-ray CT images: for drying, suction = 0 (denoted as Sample I), 40 (II), 55 (III), and 70 cmH_2O (IV); for wetting, suction = 35 (V), 20 (VI), and 0 cmH_2O (VII, resaturated). The volumetric water contents of Samples II (drying) and VI (wetting) were comparable, as were those of Samples III (drying) and V (wetting). In addition, the drying and wetting processes did not cause the samples to swell and shrink. The pore networks in the water phase for Sample IV and in the air phase for Sample VII could not be analyzed because of the limited fluid content for the image analysis.

2.4 | Measurements of mass transport parameters

Hydraulic conductivity (K), gas diffusion coefficient (D_p), and air permeability (k_a) were measured as mass transport parameters for the samples under variable saturated conditions. Triplicate measurements were performed for each mass transport parameter. The saturated and quasisaturated hydraulic conductivities (K_{sat} and K_{quasi}) of fully saturated and quasisaturated (H_2O_2 and resaturated) samples were measured using the falling head method. The obtained K_{quasi} as a function of the volume fraction of entrapped air (ω, $cm^3\ cm^{-3}$) was fitted using the model proposed by Faybishenko (1995), as follows:

$$K_{quasi} = K_0 + \left(K_{sat} - K_0\right)\left(1 - \frac{\omega}{\omega_{max}}\right)^n \quad (1)$$

where ω_{max} is the maximum ω ($cm^3\ cm^{-3}$), K_0 is the K_{quasi} at ω_{max} ($cm\ s^{-1}$), and n is the fitting parameter.

The unsaturated hydraulic conductivity (K_{unsat}) of the sand during the drying and wetting processes was measured using the suction control method (Klute & Dirksen, 1986), where different suctions were applied to the top and bottom boundaries of the column using a Marriott bottle reservoir and drain tubes, respectively. Two tensiometers were installed in the upper and lower parts of the column, and the average suction was calculated. Starting from fully saturated conditions and increasing each suction applied to the top and bottom boundaries, K_{unsat} was measured under steady water flow at each mean suction during the drying process. Following K_{unsat} measurements, at a mean suction of 60 cmH_2O during the wetting process, the applied suction was reduced to each column boundary. Diffusion chamber method was used to measure D_p for unsaturated samples during drying and wetting processes (Rolston & Moldrup, 2002), with oxygen used as a trace gas. At 20 °C, the gas diffusion coefficient in free air (D_0) was calculated to be 0.20 $cm^2\ s^{-1}$ (Currie, 1960; Glinski & Stepniewski, 1985). The k_a was also measured for the unsaturated samples by flowing air through the column at different flow rates for each sample. The k_a was calculated from Darcy's equation based on the pressure difference across the column and viscosity of air (1.86×10^{-5} Pa s) (Iversen et al., 2001). Notably, k_a was calculated in the form of intrinsic air permeability (μm^2) as a conventional expression by considering the air viscosity based on previous studies (Chief et al., 2008; Iversen et al., 2001; Tuli et al., 2005).

2.5 | X-ray CT measurements and image analysis

An X-ray CT scanner (Metrotom 1500 G1, Carl Zeiss) was used to scan the materials. The scanning was carried out at
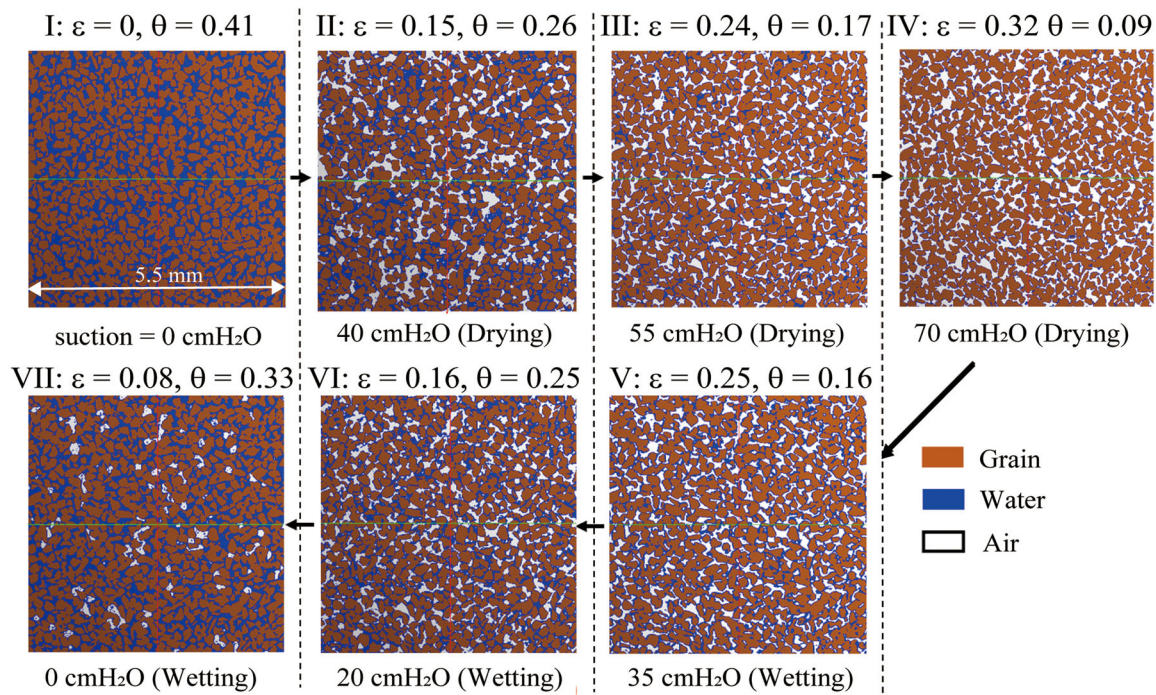
FIGURE 1 X-ray computed tomography (CT) images for Toyoura sand under drying (upper subfigures) and wetting (lower subfigures) processes. ε and θ represent air-filled porosity ($cm^3\ cm^{-3}$) and volumetric water content ($cm^3\ cm^{-3}$), respectively. The value at the bottom of each subfigure represents applied suction under drying and wetting processes

an energy level of 190 kV and 55 μA. Images (1,603 × 1,603 px, 1,502 slices) were obtained at a resolution of 10 μm. Each sample was scanned at the center position (26-mm depth from the top surface) in the repacked acrylic column. A total of 1,200 projection images were captured, with each projection having an exposure time of 8 s. Partial images (550 × 550 × 500 px) were extracted from each image for image analysis.

The scanned X-ray CT slice images were integrated to reconstruct three-dimensional images using ExFact VR (Nihon Visual Science). The X-ray CT images of each material were segmented by fitting normal distributions to the histogram of pixel intensity using the kriging algorithm to separate the grains, water, and air in the materials. Figure 1 depicts cross-sectional images of X-ray CT images of sand during the drying and wetting. With an increase in the applied suction (i.e., the drying process), the images clearly show an increase in the air-filled porosity (ε, $cm^3\ cm^{-3}$) and a decrease in the volumetric water content (θ, $cm^3\ cm^{-3}$) through the drainage of larger pores. With decreasing applied suction (i.e., wetting process) after the drying process, ε decreased. During the wetting process, air was trapped inside the material at a suction of 0 cmH_2O (lower left subfigure in Figure 1, Sample VII). Furthermore, when pairs of images with similar ε under drying and wetting processes were compared (i.e., ε is around 0.15–0.16 [II, VI] and 0.24–0.25 $cm^3\ cm^{-3}$ [III, V]), it was found that water distributions were different between drying and wetting processes, showing that water is more distributed
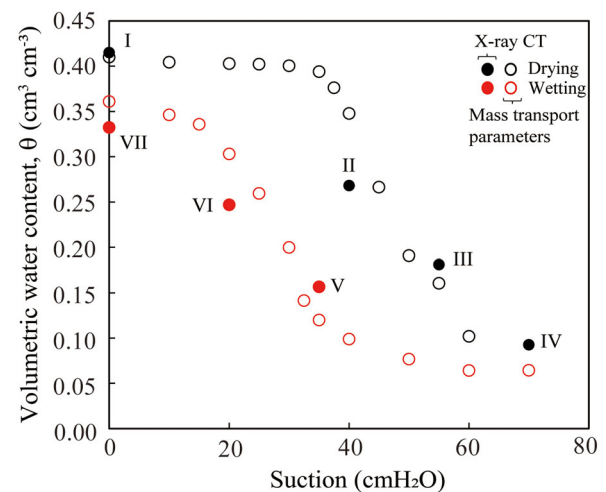
FIGURE 2 Water retention curve for Toyoura sand obtained from the samples for measuring mass transport parameters and for X-ray computed tomography (CT) images during wetting and drying processes

during the wetting process. Thus, the X-ray CT images suggest that the water retention hysteresis influences pore network characteristics in the water and air phases, even when the volume fractions are the same. Figure 2 shows a comparison of the water retention curves obtained from the samples for measuring mass transport parameters and X-ray CT image
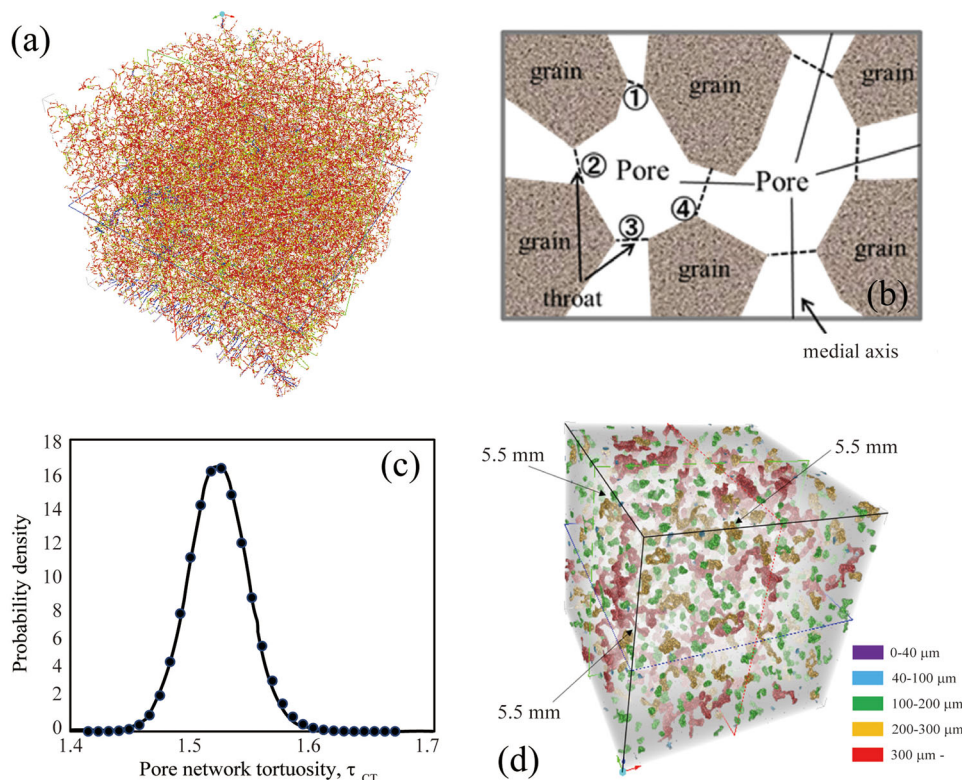
FIGURE 3 Illustrations of X-ray computed tomography (CT) analysis: (a) medial axis network, (b) calculations of equivalent pore diameter and coordination number (Hamamoto et al., 2016), (c) probability density of pore network tortuosity, and (d) characterization of entrapped air bubbles

analysis. As shown in Figure 2, the water retention curves clearly show water retention hysteresis, and the θ obtained by X-ray CT image analysis matched those obtained from the samples for the mass transport parameters.

The segmented X-ray CT images were further analyzed to characterize the pore network characteristics using ExFact Analysis (Nihon Visual Science) based on the 3DMA-Rock CT data analysis (Lindquist et al., 1996). An overview of the 3DMA package has been provided by Naveed et al. (2013) and Hamamoto et al. (2016). The CT data were analyzed by the 3DMA package in the steps of medial axis construction (Figure 3a) and medial axis analysis (Figure 3b). The medial axis of the pore space was constructed based on the burning algorithm. In the 3DMA package, a model was used to divide the pore space into nodal pores separated by throat surfaces. Throat surfaces were created by uniformly dilating a topological column from each medial axis path in the radial direction perpendicular to its length. As the dilation increased, the column grew in size until it finally hit the grain surfaces. The contact points between the column and grain surfaces created a loop that represented the minimum throat perimeter (Figure 3b). The volume of the pores separated by throat surfaces was used to calculate the size of each nodal pore. The equivalent pore diameter (d_{CT}) of each pore was determined by assuming that the pores were spherical. Pore network tortuosity (τ_{CT}) was determined by summing the length of the

medial axis voxel connecting the opposite faces and dividing this by the straight-line distance between the faces. Thus, the spatial distributions of the pore and throat sizes, coordination number (C_n, number of pores connected to a pore, four in the example of Figure 3b), and pore network tortuosity (τ_{CT}) were analyzed. The probability densities of d_{CT} and τ_{CT} were fitted using log-normal normal distribution curves for d_{CT} and normal distribution curves for τ_{CT} (Figure 3c) to obtain mean values (i.e., mean τ_{CT} and mean d_{CT}). For the X-ray CT images of the quasisaturated samples, the segmented entrapped air (i.e., bubbles) was analyzed to obtain the bubble size distributions, where each air bubble was assumed to be a sphere (Figure 3d). In addition, pore networks in the water phase (i.e., pore regions, except for air bubbles) were analyzed in the same way as unsaturated samples to obtain water-filled pore size distributions.

3 | RESULTS AND DISCUSSION

3.1 | Quasisaturated hydraulic conductivity

Figure 4 shows the measured quasisaturated hydraulic conductivity (K_{quasi}) of the resaturated and H_2O_2 samples. With increasing volume fraction of entrapped air (ω, cm³ cm⁻³), the hydraulic conductivity for both samples decreased,
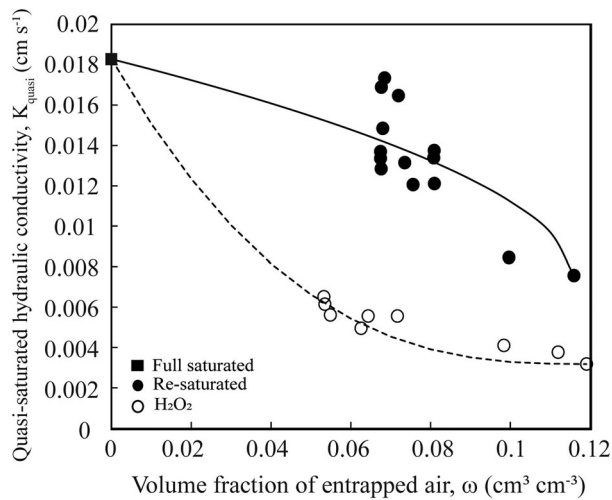
FIGURE 4 Quasisaturated hydraulic conductivity as a function of volume fraction of entrapped air (ω, cm^3 cm^{-3}). The solid and dotted lines represent model fittings by Equation 1

indicating that the entrapped air reduced the hydraulic conductivity. In this study, ω_{max} was used as the maximum ω obtained from the experiments (i.e., $\omega_{max} = 0.116$ for the resaturated samples and $\omega_{max} = 0.119$ for the H_2O_2 samples). The model well fitted the K_{quasi} value for each sample (Equation 1). The fitted n values for the resaturated and H_2O_2 samples were 0.54 and 2.7, respectively. Sakaguchi et al. (2005) proposed a relation between n and K_{sat} as $n = 214.9 K_{sat}^{0.514}$, noting that the unit of K_{sat} is m s^{-1} in the equation. Following this predictive equation, the estimated n value for the sand used in this study was 2.6, which is close to the value obtained for the H_2O_2 sample.

At the same ω, the K_{quasi} for the H_2O_2 samples was lower than for the resaturated samples. The entrapped air significantly reduced the hydraulic conductivity of the H_2O_2 samples. This finding contradicts that of a previous study by Fry et al. (1997), which found no significant difference in the reduction of K_{quasi} with the same magnitude of ω among different emplacement methods to create entrapped air (direct gas injection, injection of water supersaturated with gas, and injection of an H_2O_2 solution). Fry et al. (1997) used coarser sand grains (mean particle sizes of 0.36, 0.53, and 1.1 mm) than those used in this study. Therefore, the comparison with this study implies that finer material might be more affected by the bubble size and distribution, as well as the volume fraction of entrapped air. Figure 5a shows the pore size distribution in the water phase (water-filled pore size distribution) as determined by X-ray CT measurements on the resaturated and H_2O_2 samples with $\omega = 0.06$. Pores larger than 60 μm in the H_2O_2 samples were smaller than those in the resaturated samples. In addition, the bubble size of entrapped air in the sample with $\omega = 0.06$ showed that smaller bubbles existed in the H_2O_2 samples (Figure 5b). Consequently, smaller bubbles were distributed inside the H_2O_2 samples, resulting in full or partial clogging of the larger water-filled pores and a decrease in hydraulic conductivity. The findings also indicate how entrapped air is formed (i.e., the difference in bubble distributions and size inside saturated porous media); for example, groundwater fluctuations or biogas formation under anaerobic conditions highly influence hydraulic properties in saturated soils.

3.2 | Mass transport parameters during drying and wetting processes

The measured K_{unsat} during the drying and wetting processes is shown in Figure 6. At the same suction, a higher K_{unsat} value was obtained for the sample during the drying process than that during the wetting process. This is attributed to the increased volumetric water content during the drying process at the same suction level (Figure 2). Hydraulic conductivity as a function of volumetric water content is well known to have no hysteresis effects (Gallage et al., 2013; Mualem, 1986; Topp, 1971). In agreement with previous studies, there were no substantial differences in hydraulic conductivity during the drying and wetting processes, as shown in Figure 6b.

The measured gas diffusivity (D_p/D_0) and air permeability (k_a, μm²) as functions of suction and air-filled porosity (ε) are shown in Figure 7. Similar to hydraulic conductivity, D_p/D_0 and k_a showed significant hysteresis effects, with the wetting process showing higher gas transport parameters than the drying process due to greater air-filled porosity during the wetting process at the same suction (Figure 7a and 7b). In contrast to K_{unsat}, larger D_p/D_0 and more significant k_a were obtained during wetting rather than drying processes at the same ε. Similar findings have been reported in previous studies (Jones et al., 2003; Stonestrom & Rubin, 1989). Thus, these findings suggest fundamental differences in the water- and air-filled pore networks during the drying and wetting processes at the same fluid content. The obtained D_p/D_0 and k_a values were modeled based on Troeh et al. (1982) as follows:

$$\frac{D_p}{D_{p,max}} = \left(\frac{\varepsilon - \varepsilon_{th,D_p}}{\varepsilon_{max} - \varepsilon_{th,D_p}} \right)^a \tag{2a}$$

$$\frac{k_a}{k_{a,max}} = \left(\frac{\varepsilon - \varepsilon_{th,k_a}}{\varepsilon_{max} - \varepsilon_{th,k_a}} \right)^b \tag{2b}$$

where ε_{th,D_p} and ε_{th,k_a} are the percolation thresholds of D_p and k_a, respectively. ε_{max} is the highest ε set as ε at 70 cmH_2O (= 0.37 cm^3 cm^{-3}), and $D_{p,max}$ and $k_{a,max}$ are the measured D_p and k_a at ε_{max}, respectively. a and b are the pore structure parameters representing pore network connectivity and
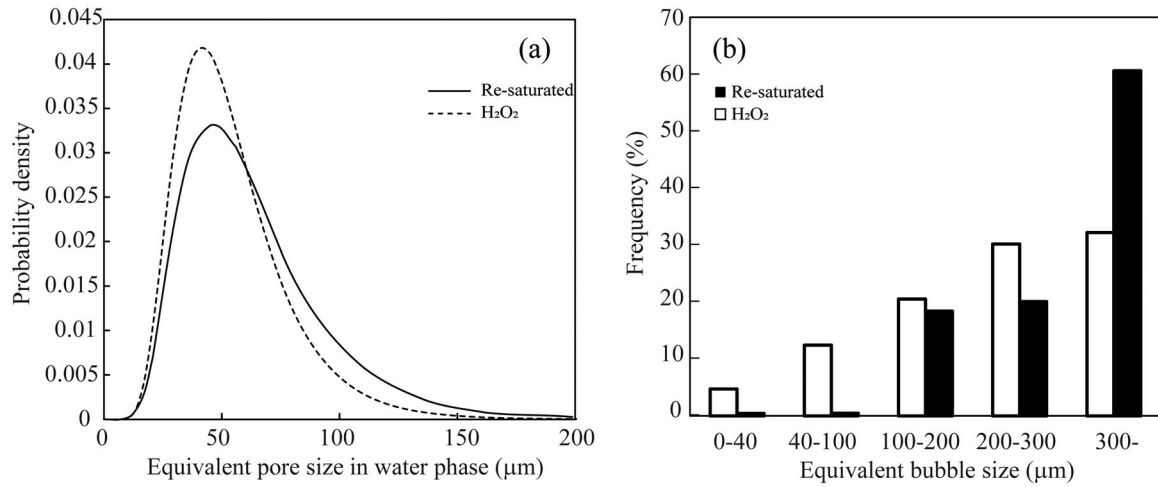
FIGURE 5 (a) Pore size distribution in water phase for resaturated and H_2O_2 samples with volume fraction of entrapped air (ω) = 0.06. (b) Volume ratio of entrapped air with different size fractions for resaturated and H_2O_2 samples with ω = 0.06
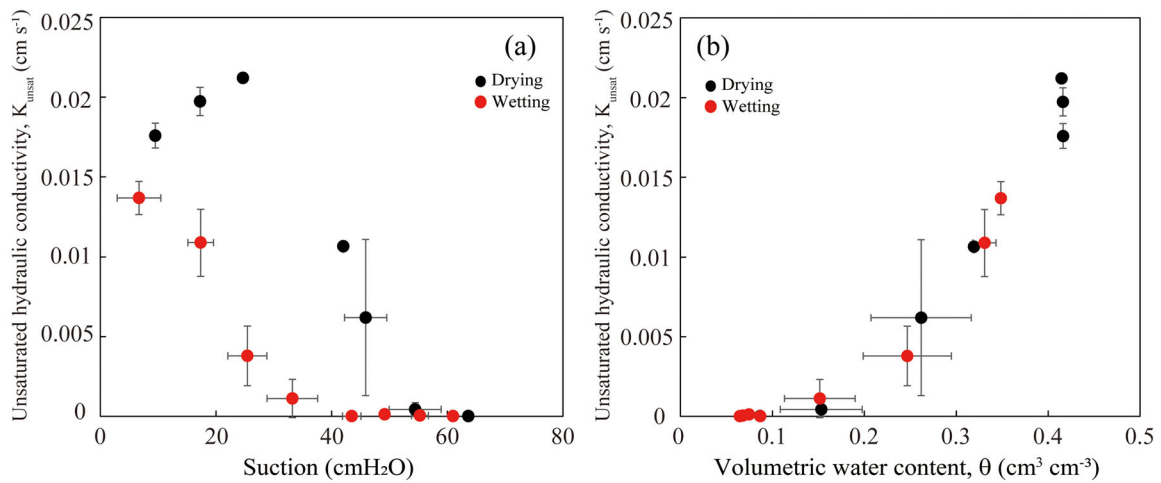

FIGURE 6 (a) Unsaturated hydraulic conductivity as a function of (a) suction and (b) volumetric water content. The error bars represent standard deviations for each sample

tortuosity, respectively. The existence of a percolation threshold due to the disconnected air phase for D_p and k_a under variably saturated conditions has been reported in many studies (Freijer, 1994; Hamamoto et al., 2011; Revil & Jougnot, 2008). ε_{th,D_p}, ε_{th,k_a}, a, and b were fitted against the measured datasets of D_p and k_a during the drying and wetting processes. The fitted models matched well with the measured D_p and k_a data, respectively, as shown in Figure 7c and 7d. The obtained fitting parameters showed that both ε_{th,D_p} and ε_{th,k_a} were zero for the drying process, whereas ε_{th,D_p} and ε_{th,k_a} for the wetting process were 0.04 and 0.07, respectively. These findings suggest the presence of an inactive, air-filled pore space during wetting. According to the water retention curve, the ε_{th} values for D_p and k_a are close to the volume fraction of entrapped air at water saturation during the wetting process (ω of approximately 0.06; Figure 2). The difference in ε_{th}

between the drying and wetting processes also indicates that the procedures for adjusting the moisture conditions of soil samples, such as repacking samples under variable moisture conditions or draining samples after presaturation, influence the inactive air-filled pore space for gas transport. The values obtained using Equation 2a were 3.33 and 1.75, and the b values in Equation 2b were 3.82 and 0.87 for the drying and wetting processes, respectively. Thus, more nonlinear behaviors for the drying processes were confirmed than for the wetting process, and a close linear behavior of k_a for the wetting process was obtained. The observed dependence of the percolation threshold and nonlinear behaviors for D_p and k_a on soil moisture history (i.e., drying and wetting) provides new insights for the future development of predictive models of gas transport parameters. The fitted models also showed that the largest difference in D_p or k_a between drying and wetting
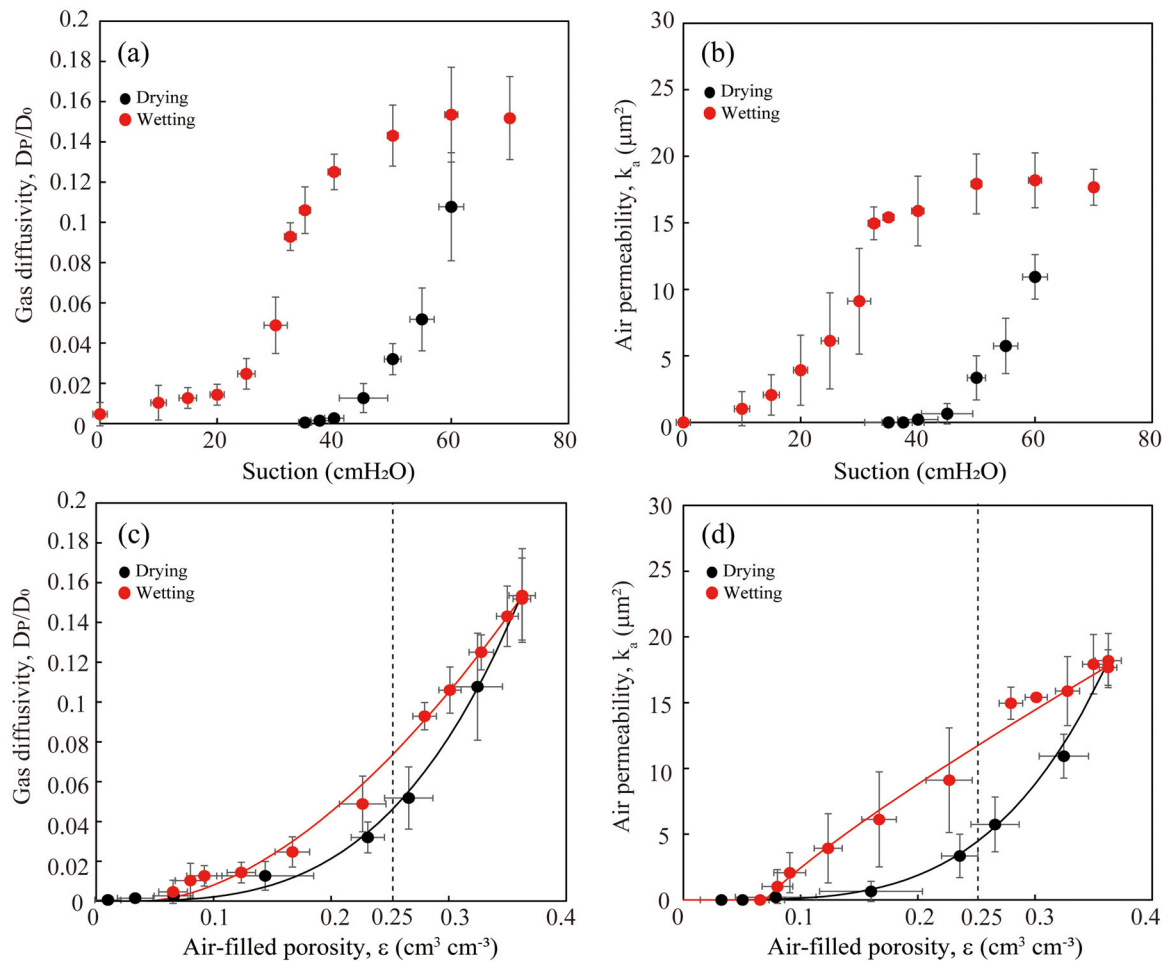
FIGURE 7 Gas diffusivity and air permeability as a function of (a, b) suction and (c, d) air-filled porosity. The error bars represent standard deviations for each sample. The solid lines in Figure 7c and 7d represent model fittings based on Equation 2a and 2b, respectively

was obtained at ε of approximately 0.25, which corresponds to approximately 60% air saturation and 40% water saturation (Figure 2).

K_{unsat} (cm s^{-1}) was converted to intrinsic water permeability (k_w, μm^2) by considering the viscosity of water (η, Pa s), density of water (ρ_w, g cm^{-3}), and gravitational acceleration (G, cm s^{-2}) as $k_w = K_{unsat}\eta/\rho_w G$ and was compared with k_a as a function of fluid content (i.e., θ for k_w and ε for k_a; Figure 8). Similar trends were observed for k_w during both the drying and wetting processes, and k_a was obtained during the drying process, whereas k_a during the wetting process showed higher values than k_w. Water permeability is controlled by the water film thickness (i.e., water content and water-filled pore size) surrounding the grains. Significant hysteresis effects on k_a, however, imply that the air-filled pore network (i.e., pore network connectivity and tortuosity, especially in larger pores), as well as air-filled porosity, regulate air transport more dramatically. Figure 8 also clearly suggests the limitation of substituting water permeability with air permeability data, which is an important issue for further modeling of multiphase mass transport.

3.3 | Water- and air-filled pore networks during drying and wetting processes

The mean pore network tortuosity (τ_{CT}) in the water and air phases derived from the X-ray CT images as a function of fluid content (i.e., ε for the air and θ for water phases) is shown in Figure 9a. In this study, the water-filled pore network under full water saturation (Sample I in Figure 2) was assumed to be identical to that in the air phase under full air saturation (i.e., completely dry condition). With the increasing fluid content, both the water- and air-phase τ_{CT} values decreased. With higher fluid content, τ_{CT} approaches 1.5, which agrees with the theoretically derived tortuosity in the air phase proposed by Marshall (1959). For the water-filled pore network, both τ_{CT} for the quasisaturated sample (Sample VII) and full water saturation (Sample I) exhibited similar values of approximately 1.5, suggesting that the presence of entrapped air had no significant effect on the tortuosity of the water-filled pore network. A slightly lower τ_{CT} in each phase was obtained during the wetting process, suggesting that almost uniform infiltration (rewetting) created fewer
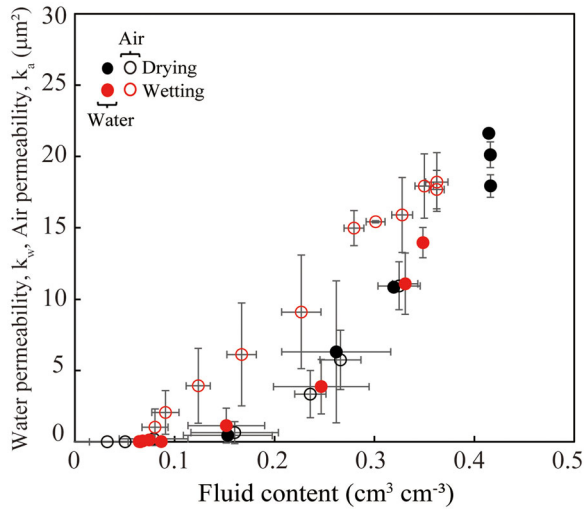
FIGURE 8 Comparisons of water permeability and air permeability under drying and wetting processes

tortuous fluid-filled pathways for the uniform sand used in this study. Following Ball (1981), the relationship between tortuosity in the air phases and gas diffusivity (D_p/D_0) can be expressed as follows:

$$\tau_{\_Dp} = \frac{L_e}{L} = \sqrt{\frac{\varepsilon}{D_p/D_0}} \qquad (3)$$

where tortuosity is defined as the ratio of the average capillary tube length, L_e, to the length of the porous medium, L, along the major flow (diffusion) axis in a tortuous (sinuous) capillary tube of uniform diameter. The $\tau_{\_Dp}$ calculated from the measured D_p/D_0 (Figure 7c) decreased with increasing fluid content (i.e., air-filled porosity), and lower values were obtained during the wetting process, as shown in Figure 9b. Similar to $\tau_{\_CT}$, $\tau_{\_Dp}$ reached 1.5 as ε increased. Thus, $\tau_{\_CT}$ for the air phase and $\tau_{\_Dp}$ exhibited similar gaseous pore network tortuosity behaviors in terms of air-filled porosity and drying–wetting processes. However, the reduction in tortuosity was more significant for $\tau_{\_Dp}$, and its value was much higher than $\tau_{\_CT}$ at a low fluid content, indicating that the actual diffusive pathways in the air phase were restricted to more tortuous but well-connected air-filled pore networks.

Figure 9c shows the mean equivalent pore size (mean $d_{\_CT}$) derived from the X-ray CT images as a function of fluid content. The mean air-filled pore size decreases as fluid content increases, whereas the mean water-filled pore size increases. This finding suggests that smaller air-filled pores contribute to air-filled pathways in the air phase under drier conditions, whereas larger water-filled pores contribute to water-filled pathways in the water phase under wetter conditions. This also explains why, at the same fluid content, the water phase had a lower mean $d_{\_CT}$ than the air phase. The mean

$d_{\_CT}$ at quasiwater saturation (Sample VII) was slight smaller than that at water saturation (Sample I), again indicating that hydraulic conductivity decreased in the presence of entrapped air (Figure 4). The mean $d_{\_CT}$ at fluid saturation (Sample I) was approximately 65 µm, corresponding to an approximate suction of 45 cmH$_2$O based on the capillary rise equation. This corresponds closely to the suction at the inflection point in the water retention curve during the drying process (Figure 2). In addition, there were no significant differences in the mean $d_{\_CT}$ values between the drying and wetting processes for the water and air phases.

Millington and Quirk (1964) assumed soil pores to be uniform, tortuous, and nonjointed tubes of similar diameter and expressed the equivalent pore size (the effective diameter of the drained pores active in leading air through the sample) by combining Fick's law and Poiseuille's law as follows:

$$d_{\_ka/Dp} = 2\sqrt{\frac{8k_a}{D_p/D_0}} \qquad (4)$$

where $d_{\_ka/Dp}$ is the effective pore size active in convective and diffusive gas transport, representing not only the pore size but also the pore connectivity. The calculated $d_{\_ka/Dp}$ based on the measured D_p/D_0 and k_a (Figure 7c and 7d) showed an increase in $d_{\_ka/Dp}$ with increasing fluid content (i.e., ε) during the drying process, suggesting that the drained smaller pores contributed to improving air-filled pore connectivity (Figure 9d). Figure 9d also shows that, under wetting conditions, $d_{\_ka/Dp}$ increased with decreasing ε above 0.12, but suddenly decreased below 0.12. This implies that water infiltration via smaller pores created a more continuous, larger air-filled pore network; however, under extremely wet conditions (i.e., $\varepsilon < 0.12$, corresponding to a suction of approximately 20 cmH$_2$O or less in the wetting curve in Figure 2), the connectivity of the pore network decreased drastically. Notably, the obtained $d_{\_ka/Dp}$ during the drying and wetting ($\varepsilon > 0.12$) processes behaved similarly to the mean $d_{\_CT}$ in the water and air phases, respectively.

The capillary rise equation calculates the minimum drained pore size (d_c, µm) for a given suction. The obtained mean $d_{\_CT}$ in the air phase at different suctions during the drying and wetting processes is compared with d_c in Figure 10a. It was assumed that the completely dry condition is achieved at suction of 100 cmH$_2$O, which corresponds to d_c of 30 µm. The mean $d_{\_CT}$ is larger than d_c because it is the mean value of the pore size distribution derived from the X-ray CT images. The mean $d_{\_CT}$ was almost 1.5 times higher than d_c under drying conditions, whereas under wetting conditions, the incremental increase in mean $d_{\_CT}$ with d_c was lower than that under the drying condition, and Sample VI ($h = 20$ cmH$_2$O) had a lower $d_{\_CT}$ value than d_c. This implies that larger pores were segmented into smaller pores in the image analysis.
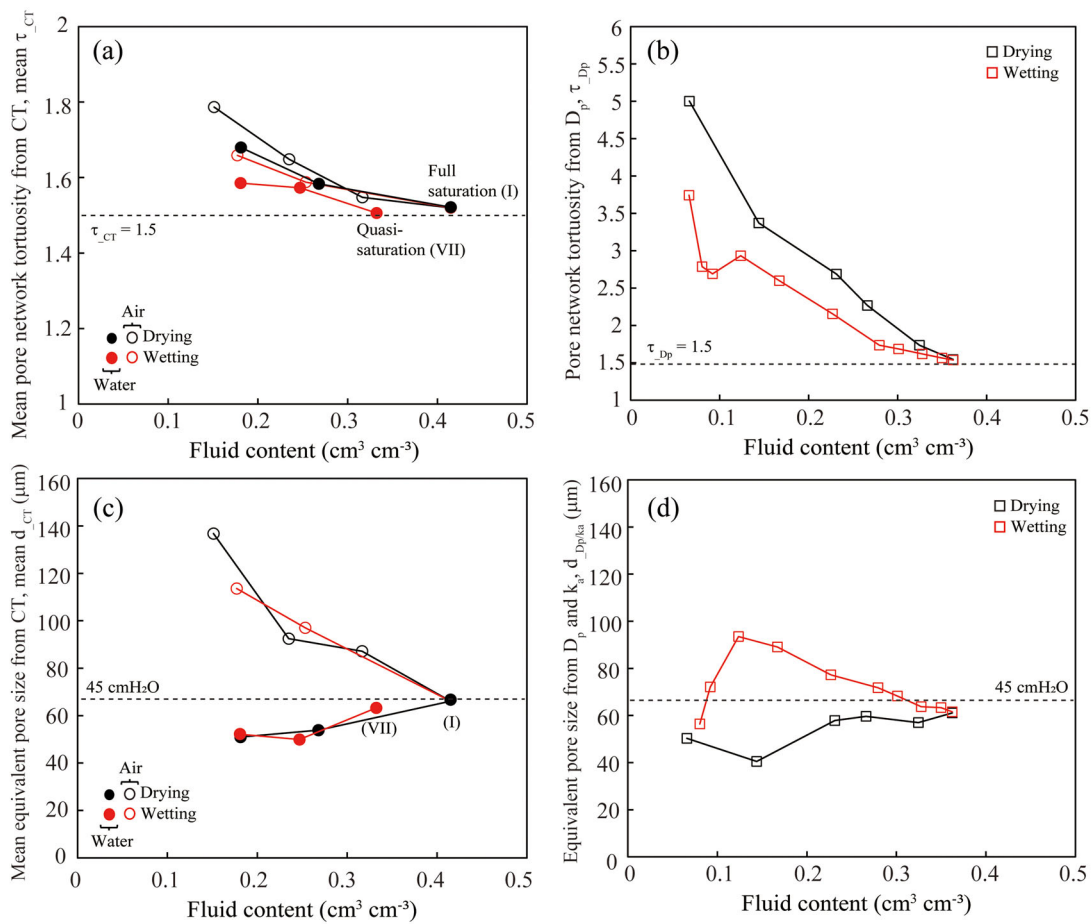
FIGURE 9 (a, b) Mean pore network tortuosity during wetting and drying (a) derived from X-ray computed tomography (CT) comparing water and air phases, and (b) from gas diffusion coefficient (D_p) for the air phase. (c, d) Mean equivalent pore size during wetting and drying (c) derived from X-ray CT comparing water and air phases, and (d) from D_p and air permeability (k_a) for the air phase
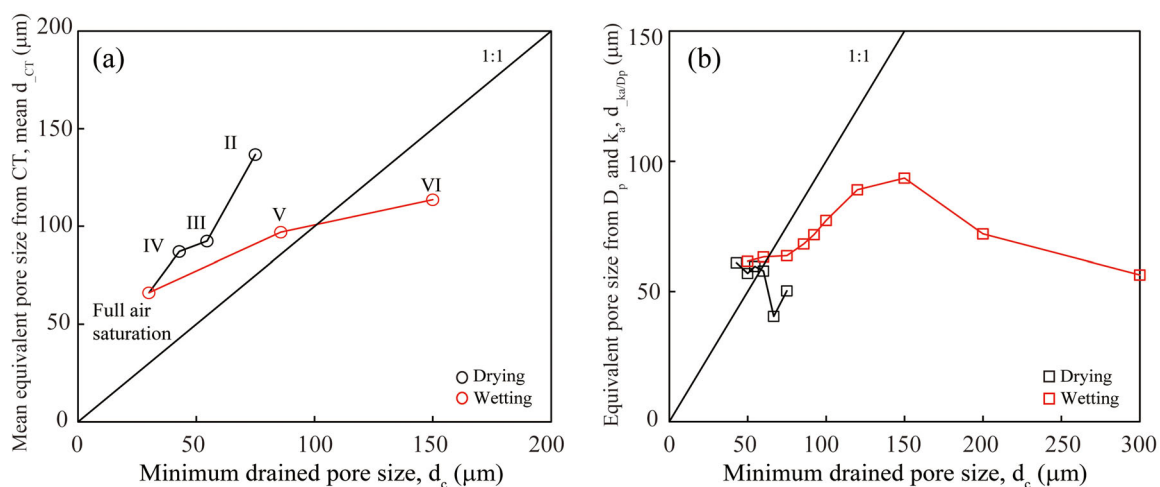

FIGURE 10 Comparisons of minimum drained pore size and (a) mean equivalent pore size derived from X-ray computed tomography (CT), and (b) equivalent pore size from gas diffusion coefficient (D_p) and air permeability (k_a), for the air phase during drying and wetting
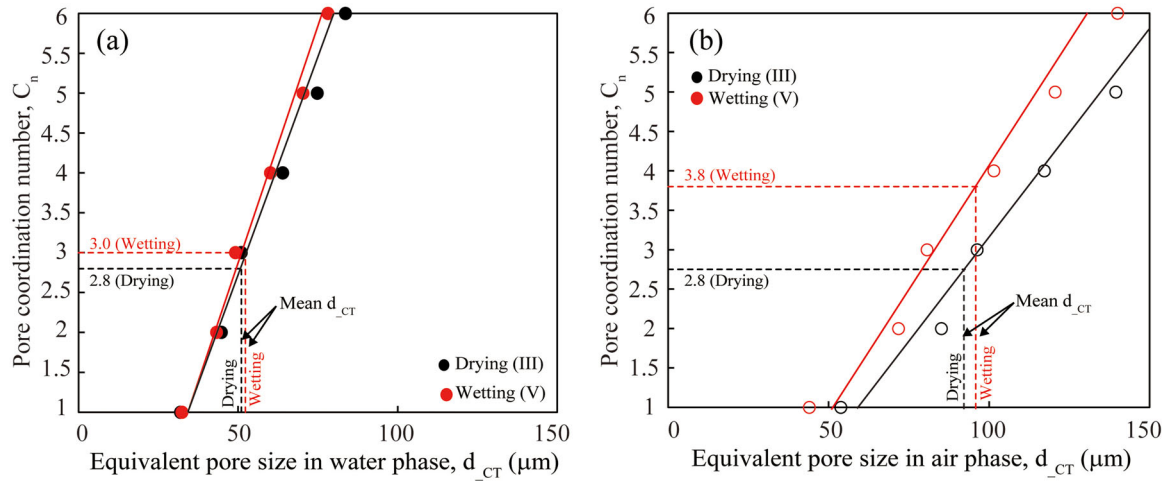
FIGURE 11 Pore coordination number as a function of equivalent pore size during wetting and drying for (a) water phase and (b) air phase

The relationship between $d_{ka/Dp}$ and d_c is shown in Figure 10b. For d_c smaller than 150 μm, corresponding to a suction of 20 cmH$_2$O, there was good agreement between $d_{ka/Dp}$ and d_c during the drying and wetting processes. However, for d_c greater than 150 μm, $d_{ka/Dp}$ under wetting conditions decreased with increasing d_c, again suggesting that soil water inhibited a larger pore network under wetter conditions.

The relationship between the equivalent pore size (d_{CT}) and pore coordination number (C_n) in each water and air phase at ε of approximately 0.25 (Sample III and V) is shown in Figure 11. For each phase, C_n increased linearly with increasing equivalent pore size, suggesting that the larger pores in each phase were well connected to other smaller pores. Figure 11 shows greater slopes for the water phase than for the air phase, indicating the presence of well-connected water-filled pore networks in the water phase due to the smaller water-filled pores surrounding the grains, contributing to pore network connectivity. In comparisons of C_n between the drying and wetting processes, higher pore coordination numbers, particularly larger pores, were obtained in the wetting process for the air phase (Figure 11b), whereas similar trends in the drying and wetting processes were obtained in the water phase (Figure 11a). At ε = 0.25, where the largest differences in D_p and k_a in the drying and wetting processes were obtained, the mean equivalent pore sizes were as follows: for the air phase, 92 μm for drying and 97 μm for wetting; for the water phase, 51 μm for drying and 52 μm for wetting. The corresponding C_n at the mean d_{CT} was significantly higher (3.8) for the wetting process in the air phase than for the drying process (2.8) (Figure 11b), whereas similar C_n values were obtained for the drying and wetting processes in the water phase (Figure 11a). This finding suggests the existence of more continuous air-filled pore networks during the wetting process, likely because smaller air-filled pores were active after drying, resulting in the formation of larger pore networks and higher gas transport

parameters, as supported by the higher k_a during the wetting process than during the drying process (Figure 7d).

4 | CONCLUSIONS

Measurements of hydraulic conductivity using quasisaturated samples prepared by different methods showed that when smaller in situ air bubbles were present inside the porous media, hydraulic conductivity was drastically reduced. This finding indicates that how entrapped air is created (i.e., bubble locations and size distributions) highly influences hydraulic properties in saturated zones, such as those affected by groundwater fluctuations. When a continuous air phase was created (i.e., an unsaturated condition), the soil moisture history and fluid content affected the fluid-filled pore networks and relevant transport parameters in each phase. In this study, gas diffusivity and air permeability showed greater values under wetting than under drying. Water permeability is controlled by the water film thickness surrounding the grains, whereas significant hysteresis effects on air permeability imply that air-filled pore networks, as well as air-filled porosity, regulate air transport more dramatically. The relationship between the pore coordination number and equivalent pore size in each phase determined using X-ray CT image analysis revealed that air-filled pore connectivity during the wetting process was higher than that during the drying process. This is likely because smaller air-filled pores are active in gas transport after the drying process, which contributes to the formation of larger pore networks, resulting in enhanced gas transport parameters during the wetting process. The findings of the water and air transport parameters, as well as the water- and air-filled pore networks under variable moisture levels, including quasisaturated and unsaturated conditions, are highly promising for further understanding the

multiphase transport of water, gas, and dissolved chemicals in soils.

AUTHOR CONTRIBUTIONS

Shoichiro Hamamoto: Formal analysis; Visualization; Methodology; Project administration; Writing – original draft. Yushi Ohko: Investigation; Visualization. Yutaka Ohtake; Investigation; Writing – review & editing. Per Moldrup: Writing – review & editing. Taku Nishimura: Writing – review & editing.

CONFICT OF INTEREST

The authors declare no conflict of interest.

ORCID

Shoichiro Hamamoto ⓘ https://orcid.org/0000-0002-6476-5585

REFERENCES

Anderson, S. H., Peyton, R. L., & Gantzer, C. J. (1990). Evaluation of constructed and natural soil macropores using X-ray computed tomography. *Geoderma*, *46*(1–3), 13–29. https://doi.org/10.1016/0016-7061(90)90004-S

Ball, B. C. (1981). Modelling of soil pores as tubes using gas permeabilities, gas diffusivities and water release. *Journal of Soil Science*, *32*, 465–481.

Baniya, A., Kawamoto, K., Hamamoto, S., Sakaki, T., Saito, T., Müller, K., Moldrup, P., & Komatsu, T. (2019). Linking pore network structure derived by microfocus X-ray CT to mass transport parameters in differently compacted loamy soils. *Soil Research*, *57*(6), https://doi.org/10.1071/SR18186

Chief, K., Ferré, T. P. A., & Hinnell, A. C. (2008). The effects of anisotropy on in situ air permeability measurements. *Vadose Zone Journal*, *7*(3), 941–947. https://doi.org/10.2136/vzj2007.0164

Currie, J. A. (1960). Gaseous diffusion in porous media. Part 2. Dry granular materials. *British Journal of Applied Physics*, *11*(8), 318–324. https://doi.org/10.1088/0508-3443/11/8/303

Dury, O., Fischer, U., & Schulin, R. (1998). Dependence of hydraulic and pneumatic characteristics of soils on a dissolved organic compound. *Journal of Contaminant Hydrology*, *33*(1–2), 39–57. https://doi.org/10.1016/S0169-7722(98)00064-3

Faybishenko, B. A. (1995). Hydraulic behavior of quasi-saturated soils in the presence of entrapped Air: Laboratory experiments. *Water Resources Research*, *31*(10), 2421–2435. https://doi.org/10.1029/95WR01654

Freijer, J. I. (1994). Calibration of jointed tube model for the gas diffusion coefficient in soils. *Soil Science Society of America Journal*, *58*(4), 1067–1076. https://doi.org/10.2136/sssaj1994.03615995005800040010x

Fry, V. A., Selker, J. S., & Gorelick, S. M. (1997). Experimental investigations for trapping oxygen gas in saturated porous media for in situ bioremediation. *Water Resources Research*, *33*(12), 2687–2696. https://doi.org/10.1029/97WR02428

Gallage, C., Kodikara, J., & Uchimura, T. (2013). Laboratory measurement of hydraulic conductivity functions of two unsaturated sandy soils during drying and wetting processes. *Soils Found*, *53*(3), 417–430. https://doi.org/10.1016/j.sandf.2013.04.004

Glinski, J., & Stepniewski, W. (1985). *Soil aeration and its role for plants*. CRC Press.

Hamamoto, S., Moldrup, P., Kawamoto, K., Sakaki, T., Nishimura, T., & Komatsu, T. (2016). Pore network structure linked by X-ray CT to particle characteristics and transport parameters. *Soils Found*, *56*(4), 676–690. https://doi.org/10.1016/j.sandf.2016.07.008

Hamamoto, S., Moldrup, P., Kawamoto, K., Wollesen de Jonge, L., Schjønning, P., & Komatsu, T. (2011). Two-region extended archie's law model for soil air permeability and gas diffusivity. *Soil Science Society of America Journal*, *75*(3), 795–806. https://doi.org/10.2136/sssaj2010.0207

Iversen, B. V., Schjønning, P., Poulsen, T. G., & Moldrup, P. (2001). In situ, on-site and laboratory measurements of soil air permeability: Boundary conditions and measurement scale. *Soil Science*, *166*(2), 97–106. https://doi.org/10.1097/00010694-200102000-00003

Jones, S. B., Or, D., & Bingham, G. E. (2003). Gas Diffusion measurement and modeling in coarse-textured porous media. *Vadose Zone Journal*, *2*(4), 602–610. https://doi.org/10.2136/vzj2003.6020

Klute, A., & Dirksen, C. (1986). Hydraulic conductivity and diffusivity: Laboratory methods. In A. Klute (Eds.), *Method of soil analysis: Part 1. Physical and mineralogical methods* (SSSA Book Series 5, pp. 687–733). ASA and SSSA. https://doi.org/10.2136/sssabookser5.1.2ed.c28

Lindquist, W. B., Lee, S. M., Coker, D. A., Jones, K. W., & Spanne, P. (1996). Medial axis analysis of void structure in three-dimensional tomographic images of porous media. *Journal of Geophysical Research, B: Solid Earth*, *101*(4), 8297–8310. https://doi.org/10.1029/95jb03039

Lindquist, W. B., Venkatarangan, A., Dunsmuir, J. R., & Wong, T. (2000). Synchrotron X-ray tomographic images. *Journal of Geophysical Research*, *105*, 509–521.

Marinas, M., Roy, J. W., & Smith, J. E. (2013). Changes in entrapped gas content and hydraulic conductivity with pressure. *GroundWater*, *51*(1), 41–50. https://doi.org/10.1111/j.1745-6584.2012.00915.x

Marshall, T. J. (1959). The diffusion of gases through porous media. *Journal of Soil Science*, *10*, 79–82.

Millington, R. J., & Quirk, J. P. (1964). Formation factor and permeability equations. *Nature*, *202*, 143–145. https://doi.org/10.1038/202143a0

Mualem, Y. (1986). Hydraulic conductivity of unsaturated soils: Prediction and formulas. In A. Klute (Eds.), *Method of soil analysis: Part 1. Physical and mineralogical methods* (SSSA Book Series 5, pp. 799–823). ASA and SSSA. https://doi.org/10.2136/sssabookser5.1.2ed.c31

Müller, K., Katuwal, S., Young, I., McLeod, M., Moldrup, P., Wollesen de Jonge, L., & Clothier, B. (2018). Characterising and linking X-ray CT derived macroporosity parameters to infiltration in soils with contrasting structures. *Geoderma*, *313*, 82–91. https://doi.org/10.1016/j.geoderma.2017.10.020

Naveed, M., Hamamoto, S., Kawamoto, K., Sakaki, T., Takahashi, M., Komatsu, T., Moldrup, P., Lamandé, M., Wildenschild, D., Prodanović, M., & Wollesen de Jonge, L. (2013). Correlating gas transport parameters and x-ray computed tomography measurements in porous media. *Soil Science*, *178*(2), 60–68. https://doi.org/10.1097/SS.0b013e318288784c

Rachman, A., Anderson, S. H., & Gantzer, C. J. (2005). Computed-tomographic measurement of soil macroporosity parameters as affected by stiff-stemmed grass hedges. *Soil Science Society of America Journal*, *69*(5), 1609–1616. https://doi.org/10.2136/sssaj2004.0312

Revil, A., & Jougnot, D. (2008). Diffusion of ions in unsaturated porous materials. *Journal of Colloid & Interface Science*, *319*(1), 226–235. https://doi.org/10.1016/j.jcis.2007.10.041

Rolston, D. E., & Moldrup, P. (2002). Gas diffusivity. In J. H. Dane & G. C. Topp (Eds.), *Methods of soil analysis, Part 4: Physical methods* (SSSA Book Series 5, pp. 1113–1139). ASA and SSSA. https://doi.org/10.2136/sssabookser5.4.c45

Ronen, D., Berkowitz, B., & Magaritz, M. (1989). The development and influence of gas bubbles in phreatic aquifers under natural flow conditions. *Transport in Porous Media*, *4*(3), 295–306. https://doi.org/10.1007/BF00138041

Ryan, M. C., MacQuarrie, K. T. B., Harman, J., & McLellan, J. (2000). Field and modeling evidence for a "stagnant flow" zone in the upper meter of sandy phreatic aquifers. *Journal of Hydrology*, *233*(1–4), 223–240. https://doi.org/10.1016/S0022-1694(00)00236-5

Sakaguchi, A., Nishimura, T., & Kato, M. (2005). The effect of entrapped air on the quasi-saturated soil hydraulic conductivity and comparison with the unsaturated hydraulic conductivity. *Vadose Zone Journal*, *4*, 139–144. https://doi.org/10.2136/vzj2005.0139

Stonestrom, D. A., & Rubin, J. (1989). Air permeability and trapped-air content in two soils. *Water Resources Research*, *25*(9), 1959–1969. https://doi.org/10.1029/WR025i009p01959

Topp, G. C. (1971). Soil water hysteresis in silt loam and clay loam soils. *Water Resources Research*, *7*(4), 914–920. https://doi.org/10.1029/WR007i004p00914

Troeh, F. R., Jabro, J. D., & Kirkham, D. (1982). Gaseous diffusion equations for porous materials. *Geoderma*, *27*(3), 239–253. https://doi.org/10.1016/0016-7061(82)90033-7

Tuli, A., Hopmans, J. W., Rolston, D. E., & Moldrup, P. (2005). Comparison of air and water permeability between disturbed and undisturbed soils. *Soil Science Society of America Journal*, *69*(5), 1361–1371. https://doi.org/10.2136/sssaj2004.0332